Aerospace Science and Technology 167 (2025) 110694

Contents lists available at ScienceDirect

Aerospace Science and Technology

journal homepage: www.elsevier.com/locate/aescte

Deployable mesh reflector antenna for global navigation satellite system radio occultation within 1U CubeSat form factor

Gagyeong Park, Dong-Wook Yang, Min-Woo Oh, Jang-Soo Chae, Hyosang Yoon, Jae-Hung Han, Dae-Young Lee *

Department of Aerospace Engineering, Korea Advanced Institute of Science and Technology (KAIST), Daejeon, 34141, Republic of Korea

ARTICLE INFO

Edited by: Roberto Sabatini

Keywords:
CubeSat
GNSS-RO
Deployable antenna
Mesh reflector antenna
Cross-axis folding hinge

ABSTRACT

The Global Navigation Satellite System Radio Occultation (GNSS-RO) technique is recognized as an effective method for atmospheric observation. However, the cost of deploying and operating satellite constellations remains a significant challenge. CubeSats offer a promising alternative due to their cost efficiency and mission flexibility, but their small form factor limits antenna aperture size, resulting in reduced antenna gain—a critical factor for GNSS-RO performance. This study presents a 0.5-meter deployable mesh reflector antenna designed to be stowed within a standard 1 U CubeSat (10 cm × 10 cm × 10 cm). The proposed design employs a central hub with a cross-axis folding and locking mechanism that enables both a high storage ratio and reliable deployment. The prototype demonstrates high geometric stability, achieving a deployed surface accuracy with a root mean square error of 5.41 mm after the first deployment. The measured directivity reaches 13.07 dBi, representing a 61 % improvement over a commercial GNSS-RO patch antenna.

1. Introduction

1.1. Background about GNSS-RO satellites

Over the past few decades, global warming has led to abnormal climate phenomena. Its frequency and intensity have increased for natural disasters such as heavy snowfall, floods, and droughts, negatively affecting human life [1]. Consequently, monitoring the Earth's atmosphere has become essential for minimizing damage to life and property.

Global Navigation Satellite System Radio Occultation (GNSS-RO) is an atmospheric observation technique utilizing satellites that measure GNSS radio signals refracted as they pass through the atmosphere [2]. Since the magnitude of refraction depends on temperature and water vapor concentration, atmospheric profiles can be derived.

Various satellites have been launched to support GNSS-RO missions [3], such as GRACE [4], CHAMP [5], FORMOSAT-3 / COSMIC [6], MetOp [7], and FengYun satellites [8]. While these missions commonly employ satellites heavier than 50 kg, CubeSats are a promising platform for GNSS-RO, offering advantages such as lower cost, smaller payloads [9], and improved coverage, [10].

CubeSat's small size and reduced cost allow satellite constellations, providing comprehensive global coverage and frequent data updates for atmospheric monitoring [11]. Furthermore, their modular design supports rapid customization, meeting specific mission requirements [12]. The PSSCT-2 nanosatellite is an example of applying a CubeSat to a GNSS-RO mission [13]. Small satellites of commercial companies, such as Spire [14] and PlanetiQ [15], are also launched. They demonstrate the capability to deliver reliable atmospheric data with reduced resources.

Antenna gain is a critical factor in GNSS-RO. High antenna gain is needed for the reliable detection of weak signals that pass through atmospheric layers [16]. Conventional large GNSS-RO satellites employ choke ring antennas or patch antennas, which have a high gain of around 10 dB [17]. However, achieving high gain becomes challenging at the CubeSat scale due to the limited volume, which leads to degraded retrieval quality [15]. Although various techniques have been proposed, such as those utilizing metamaterials [18], opportunities for advancement persist.

The dual patch antenna of PSSCT-2 nanosatellite, whose overall dimensions are 76 mm × 76 mm × 10 mm, exhibits a gain of 6.2 dBic at L1 (1.57 GHz) frequency. Spire's three-patch antenna for polarimetric radio occultation (PRO) has a peak gain of 9.75 dB, but its structure is

* Correspondence author at. Department of Aerospace Engineering, Korea Advanced Institute of Science and Technology (KAIST), 291, Daehak-ro, Yuseong-gu, Daejeon, Republic of Korea, 34141.

E-mail address: ae_dylee@kaist.ac.kr (D.-Y. Lee).

https://doi.org/10.1016/j.ast.2025.110694
Received 16 February 2025; Received in revised form 7 July 2025; Accepted 23 July 2025
Available online 29 July 2025

Nomenclature

Acronyms

GNSS-RO	Global Navigation Satellite System Radio Occultation
1U	A cube with dimensions of 10 cm × 10 cm × 10 cm.
SMA	Shape memory alloy
RMS	Root mean square
PET	Polyethylene terephthalate
VNA	Vector network analyzer
S_{11}	Return loss
AR	Axial ratio
RHCP	Hand-circular polarization
LHCP	Left-hand-circular polarization
HPBW	Half-power beam width

Variables

d	Diameter of the reflector
λ	Wavelength
ε_{ap}	Aperture efficiency
δ_{rms}	Loss of the gain caused by RMS surface error
σ_{rms}	RMS surface error
{s}	Fixed reference frame
{b}	Body frame of the ribs in the deployed state
{c}	Body frame of the ribs in the stowed state
C	Position of an arbitrary point on the rib with respect to the frame {s} in the deployed state
C′	Rotated point **C** for the stowed state with respect to the frame {s}
R	Rotation matrix that rotates ribs
$r(\phi)$	Polar coordinates of ribs in stowed state according to angle ϕ
N	The number of ribs
a	Spacing between stowed ribs
D_{hs}	Hub diameter in stowed state
K	Gaussian curvature of gore
κ_2	Principal curvature in the radial direction of gore
κ_1	Principal curvature in the circumferential direction of gore
R_C	Curvature radius on each side of rib's cross-section
W	Width of rib
L_i	Length of gore's edge closest to the hub
L_{i_min}	Minimum length of gore's edge closest to the hub
L_o	Length of gore's edge furthest from the hub
L_s	Length of curved sides of gore
f	Focal length of reflector
R	Radius of reflector in the top view.
H	Angular impulse
I	Moment of inertia
m	Mass of 3 U CubeSat
a	Length of the CubeSat perpendicular to the axis of rotation
b	Width of the CubeSat perpendicular to the axis of rotation
$\Delta\omega$	Angular velocity
n	Total number of points for surface accuracy measurement
Δz	Error between the z-axis values of the measured points and the ideal parabolic surface

incompatible with a modular 1 U (10 cm × 10 cm × 10 cm) payload envelope. This situation motivated our exploration of a deployable antenna concept which can achieve high gain over 10 dBi while stowing compactly into a 1 U module.

1.2. CubeSat-oriented antennas

The paradigm for space missions has shifted from large satellites toward small, cost-effective CubeSat platforms. This trend enables new mission architectures, including large constellations for global coverage, but introduces the significant challenge of achieving high antenna gain within severely limited volume constraints.

To overcome this limitation, deployable antennas that can be stowed compactly for launch have become a primary area of research. One major approach is the deployable reflector antennas to create a large effective aperture. The studies focus on various foldable structures using metal mesh, such as tension truss antenna [19], fold rib antenna [20], wrapped rib antenna [21], which are primarily optimized for high-frequency bands.

Other strategies explore self-deploying radiating structures, including lightweight and reliable helical antennas [22], and fully 3D-printed, self-deployable Yagi–Uda phased arrays that achieve significant gain and beam steering without needing any actuators [23]. Furthermore, studies have also focused on developing reconfigurable origami-inspired antenna which can switch between omnidirectional and high-gain modes [24], a compact S-band antenna system that utilizes the satellite structure itself via characteristic modes theory [25].

This review indicates that the advancement of deployable apertures is the dominant strategy for meeting the increasing demand for high gain in future CubeSat missions. While deployable helical antennas and novel approaches show promise, deployable reflector antennas are a well-established and straightforward way to create large effective apertures for missions demanding high performance.

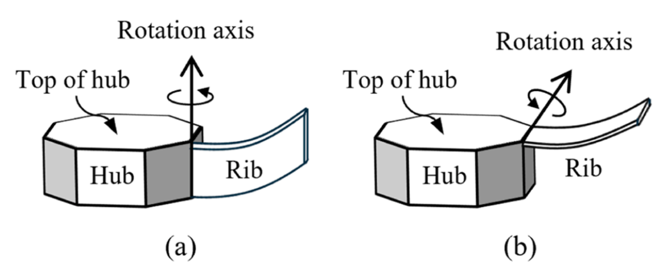

Fig. 1. Connection types between the hub and the rib. (a) Vertical connection to the top of the hub. (b) Horizontal connection to the top of the hub.

1.3. Conventional deployable mesh reflector antennas

The mesh antenna is a widely utilized type in space applications due to its lightweight and high storage ratio which is usually defined as the ratio of the reflector's deployed diameter to its stowed diameter [26]. There are diverse types of mesh antennas: Tension truss antenna [27]; Fold rib antenna [28]; Wrapped rib antenna [29].

The tension truss antennas are constructed using numerous cables. The parabolic surface is formed by applying constant tension to the cable network. The structure has a high storage ratio and high surface accuracy, and research is currently being conducted to further improve the accuracy [30]. However, the cable network is significantly complex, which increases the risk of the cables becoming tangled.

The fold rib antenna features a simple, umbrella-shaped deployable mechanism, but has the disadvantage of a low storage ratio in height due to structural limitations. There are research papers to address this problem by using multiple rotating joints on each rib [31]. However, the crease lines may potentially compromise the integrity of the mesh. Additionally, foldable mesh reflector antennas utilizing elastic shape memory alloy (SMA) has been explored, which yields a lightweight and self-recoverable mechanism without permanent deformation [32]. However, this approach has a relatively low storage ratio despite its advantages.

The wrapped rib antenna has flexible ribs that can be rolled into a spiral shape around a hub to be stowed. The elastic potential energy of deformed ribs ensures a simple deployment mechanism. The wrapped rib antenna has a high storage ratio in both diameter and height, which can be suitable for CubeSat applications. As shown in Fig. 1(a), the ribs are vertically connected based on the top of the hub to ensure that the ribs wrap around the hub, reducing interference between the ribs. However, while rib's flexibility offers advantages for efficient stowage, its high rigidity is also essential to maintain the deployed shape.

In the previous research, the composite materials are used, and the angle between the hub and the rib is adjusted to resolve the dilemma by reducing the stress of the rib's root in the stowed state [33]. Also, a reinforcement structure is installed to apply tension in the direction opposite to the wrapping direction in the deployed state [34]. However, this structure still makes the ribs vulnerable to bending in the wrapping direction, and installing additional structures is difficult for CubeSat antenna systems due to the small volume.

Basically, the robustness in the wrapping direction can be addressed by a horizontal connection between the rib and the hub as shown in Fig 1 (b). But this configuration presents a challenge in the stowage process. Thus, technological advancements that integrate the high storage ratio of the vertical configuration with the rigidity of the horizontal configuration are required.

1.4. Proposed deployable mesh reflector mechanism

The presented antenna is anticipated to be employed to acquire GPS signals modulated with Binary Phase Shift Keying, Rate 1 (BPSK-R(1)). Based on prior research, a received signal power of approximately –120 dBm for GPS L1 signals is indicated with a 4 dBi antenna [35]. The received signal power can be increased to −114 dBm by using antennas with the gain of 10 dBi, which enhancement facilitates reliable operation across most GNSS-RO scenarios.

For the deployable reflector antennas, it is essential to preserve the antenna's shape in the deployed state to ensure geometrical stability. In other words, it requires high surface accuracy, which is an evaluation metric that quantifies the deviation of the reflector's shape from an ideal parabolic surface. A larger reflector is better for increasing gain, but storing the antenna in a compact volume while ensuring high surface accuracy presents a significant design challenge. Structures with high compressibility often require multiple deformable or foldable components, increasing the risk of distortion and compromising geometric stability after deployment. Therefore, this paper focuses on researching the deployable mesh reflector, as it represents a critical path toward enabling the next generation of CubeSat applications.

In this paper, a 1U-scale deployable mesh reflector for GNSS-RO CubeSat is presented. The proposed mechanism addresses competing demands by using cross-axis folding hinges applied to the central hub. In the stowed state, each rib's bending axis is vertical to the top of the hub, which achieves efficient wrapping and high storage ratio. In the deployed state, the ribs pivot so that the top of the hub becomes parallel to each rib. This orthogonal shift allows a larger contact area with the mesh, mitigating distortion and preserving the antenna's shape once deployed, thus enhancing its geometrical stability.

Experimental results show that the proposed system can deploy from a 1 U volume into a 0.5 m-diameter reflector antenna, and the measured surface accuracy exhibits a root mean square (RMS) error of 5.41 mm even after the first deployment. Radiation pattern measurements confirm a peak directivity of 13.07 dBi for the proposed reflector antenna, which closely approaches 14.14 dBi of an ideal, non-deployable solid reflector. It also represents a 61 % improvement in directivity compared to the commercial CubeSat patch antennas of Spire.

Table 1
Specifications of the proposed antenna.

Frequency band	L1 band (1.57 GHz)
Directivity	> 13.01 dBi
RMS surface error	< 9.55 mm (λ/20 @1.57 GHz)
Deployed diameter	500 mm
Stowed diameter	< 100 mm
Focal ratio	0.4

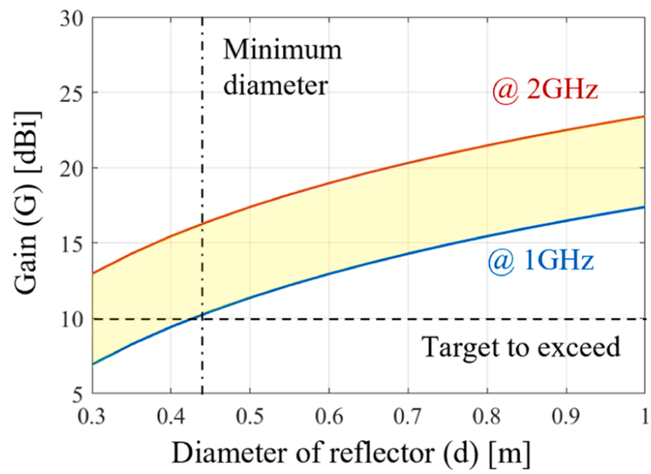

Fig. 2. Gain depending on the diameter of the reflector when the aperture efficiency is 0.5.

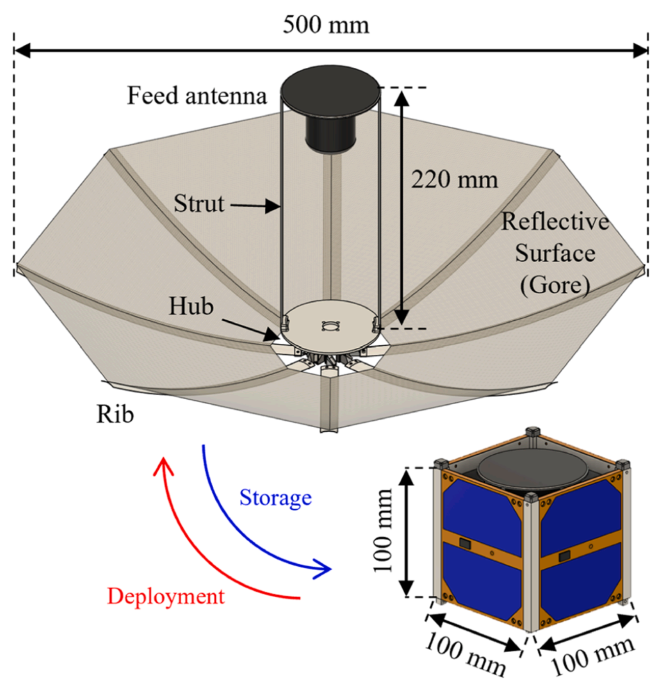

Fig. 3. Design of the proposed deployable mesh reflector antenna.

2. Specifications of antenna

The specifications to be achieved by the deployable reflector antenna are summarized in Table 1. An axisymmetric reflector configuration and a front-feed antenna were selected as the feed type for the prototype and the focal ratio of 0.4 is selected arbitrarily. The diameter of the reflector was determined considering the gain. The gain, G, of a parabolic

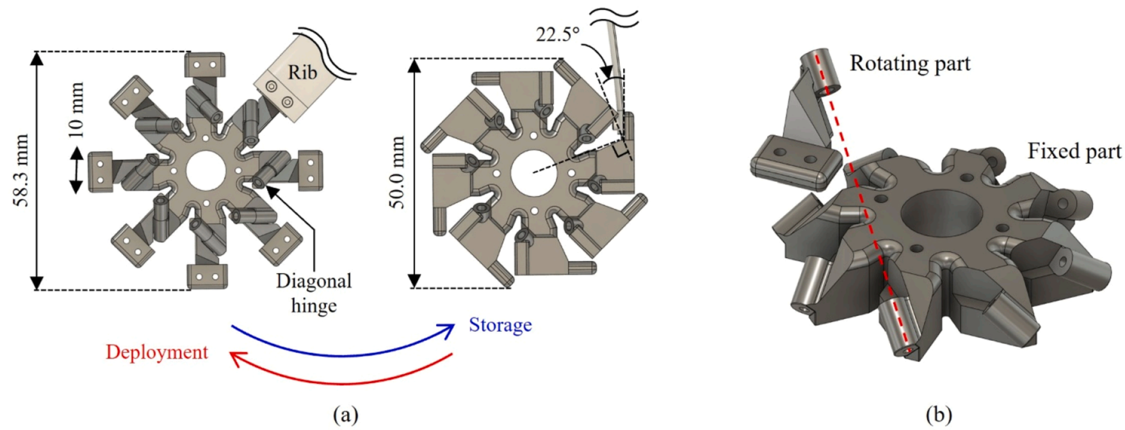

Fig. 4. (a) Design of the hub in deployed and stowed state. (b) Assembly process of hinge structure.

reflector antenna is given by:

$$G = 10\log\left(\left(\frac{\pi d}{\lambda}\right)^2 \varepsilon_{ap}\right) \quad (1)$$

where d is the diameter of the reflector, λ is wavelength, and $\varepsilon_{ap}$is the aperture efficiency [36]. Fig. 2 represents the antenna gain according to the diameter of a reflector in L-band (1–2 GHz) which includes the frequencies of GNSS signals. The gain increases as the size of the reflector increases and the diameter should be 0.5 m or greater to obtain a gain of over 10 dBi.

Fig. 3 shows the proposed mesh reflector antenna system in the deployed and stowed state. The reflector consists of a hub, rib, and reflective surface that is segmented into eight gores. For the feeding mechanism, the RF cable runs from the feed antenna down to the hub along the strut and then passes through a central hole in the hub component to connect with the spacecraft's receiver. The whole antenna system can be stowed within a 1 U, which includes a catapulting spring positioned at the base.

The value of the minimum directivity is determined to be 13.01 dBi, based on a conservative assumption of an aperture efficiency of 0.5 where the target antenna gain is 10 dB. While both directivity and gain are fundamental metrics for antenna evaluation, they represent distinct aspects of performance. Gain accounts for the overall efficiency of the antenna system, incorporating aperture efficiency, and impedance mismatch. In contrast, directivity is determined by the antenna's geometry, which is independent of the dissipative loss. The main focus of this study is the geometric integrity of the proposed deployment mechanism. Therefore, directivity has been chosen as the principal performance criterion.

Additionally, the target RMS surface error was set to be <9.55 mm (λ/20 at GPS L1) based on required guideline [37]. The antenna's performance exhibits a non-linear sensitivity to RMS surface error tolerance according to the Ruze equation [36]:

$$\delta_{rms} = 10\log\left(e^{-\left(\frac{4\pi\sigma_{rms}}{\lambda}\right)^2}\right) \quad (2)$$

where δ_{rms} is the loss of the gain caused by RMS surface error, σ_{rms} is RMS surface error, and λ is wavelength. While the target of 9.55 mm corresponds to a predictable 1.70 dB loss, any degradation beyond this point is significant. An increase in RMS error to 10.55 mm and 11.55 mm elevates the predicted loss to 2.08 dB and 2.50 dB, respectively. Even a millimeter-scale inaccuracy could result in a crucial reduction in antenna gain. Therefore, the proposed deployment mechanism provides geometrical stability to minimize surface deviations due to deployment or operational conditions.

3. Mechanism of deployable mesh reflector antenna

The hub, ribs, and gores are the main components of the reflector. The hub contains the cross-axis folding hinge, which changes the angle of the rib. When the antenna is deployed, the top of the hub and the rib are connected in parallel. On the other hand, they are in vertical contact when the antenna is stowed. The rib serves as a frame, which is required to be flexible enough to be rolled up, yet rigid enough to maintain the form of the reflector after deployment. The rib has curvatures in two directions, and the stiffness is appropriately adjusted by changing the curvature of the cross-section. Lastly, the gore, a piece of the reflective surface, needs to be designed precisely to ensure uniform tension between the ribs, thereby increasing surface accuracy. The antenna performance can be improved by ensuring accurate fabrication of these components.

In subSection 3. 1, the geometry of the hub is analyzed based on coordinates, and the locking mechanism is proposed, which ensures that the reflector's shape in the deployed state is maintained. In subSection 3. 2, the geometry of the rib is presented, and the selection of the ribs' cross-sectional parameters based on functional requirements is also discussed. In subSection 3. 3, a method is presented for defining the gore's geometry by calculating its boundary lengths and the angles between its respective sides.

3.1. Geometry of hub

The cross-axis folding hinge is applied to the hub for rotating the ribs to desired positions as shown in Fig. 4(a). The geometric stability, which is quantitatively defined by surface accuracy, can be maximized when the reflector is deployed by preventing the transition of ribs in the wrapping direction. Furthermore, the design enhances storage ratio in the stowed state. When the antenna is stowed, the ribs are wrapped around the central hub, inducing significant bending stress. The angle that each rib root forms with the tangent of the hub is a critical design parameter because it determines the initial bend radius. For the proposed mechanism, this angle is set to 22.5° based on the geometry of the hub mechanism. This specific geometry provides a gradual curvature at the start of the wrap, reducing stress concentration at the rib's root and preventing permanent deformation.

The hub mechanism is designed to adjust the orientation of the ribs with a single rotation to enhance reliability, utilizing the cross-axis folding hinge. The hub is divided into a rotating part and a fixed part as shown in Fig. 4(b). Both parts are fastened using bolts (hinge pin). The holes of the fixed part are tap-drilled to match the bolt specifications. The holes of the rotating parts are loosely fitted to the bolt, featuring a

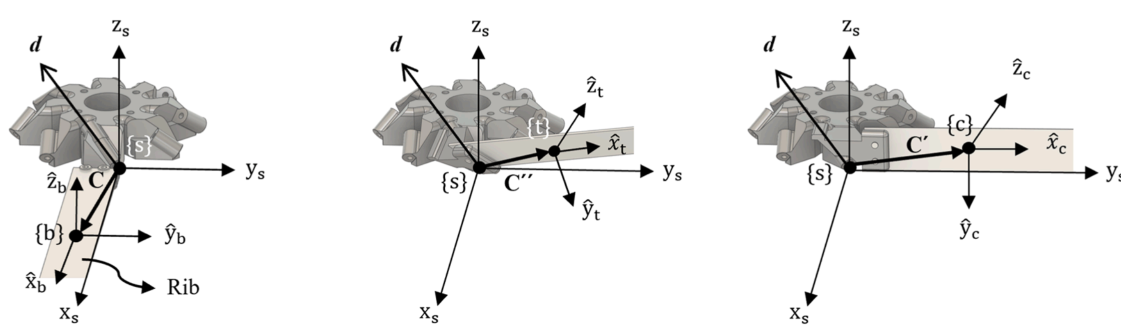

Fig. 5. Change in the orientation of a rib in Cartesian coordinates from deployment to stowage.

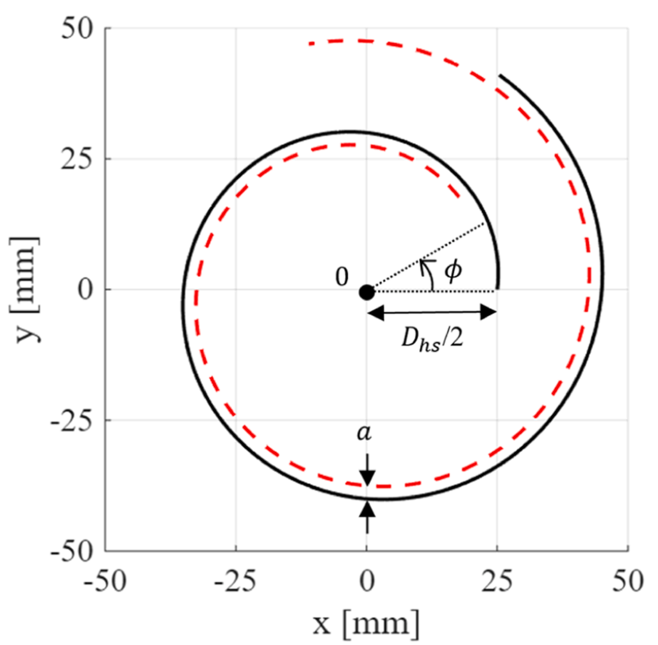

Fig. 6. Configuration of two ribs in stowed state which is stowed in a 100 mm x 100 mm square.

nominal gap of 0.2 mm at the corresponding interface. Consequently, the ribs connected to the rotating parts can achieve varying angles with respect to the reflective surface by rotating together.

Fig. 5 illustrates the positional changes of the ribs in Cartesian coordinates with a fixed reference frame {s} where the origin is located at the center of the hinge pin's base. From this origin, the vertical direction from the ground is defined as the z_s-axis, pointing upward. The y_s-axis is aligned along the length of the deployed rib in the top view. The x_s-axis is set perpendicular to the deployed rib's direction, completing the conventional coordinate system. The body frames of the ribs in the deployed and stowed state are denoted {b} and {c}, respectively. The orientation of the rib changes significantly with respect to the fixed reference frame {s} between its two states. The rib is parallel to the XY-plane in the deployed state, but perpendicular to the XY-plane in the stowed state. The components of **C** define the position of an arbitrary point on the rib with respect to the frame {s}. Assuming $\mathbf{C} = (C_x,\ C_y,\ C_z)$ is the origin of the body frame in the deployed state and is expressed in the reference frame {s}, and $\mathbf{C}' = (-C_z,\ C_x,\ -C_y)$ represents rotated point **C** in the stowed state. The relationship between these points is given by (3) where $\mathbf{R} \in SO(3)$ is a rotation matrix [38].

$$C' = RC \tag{3}$$

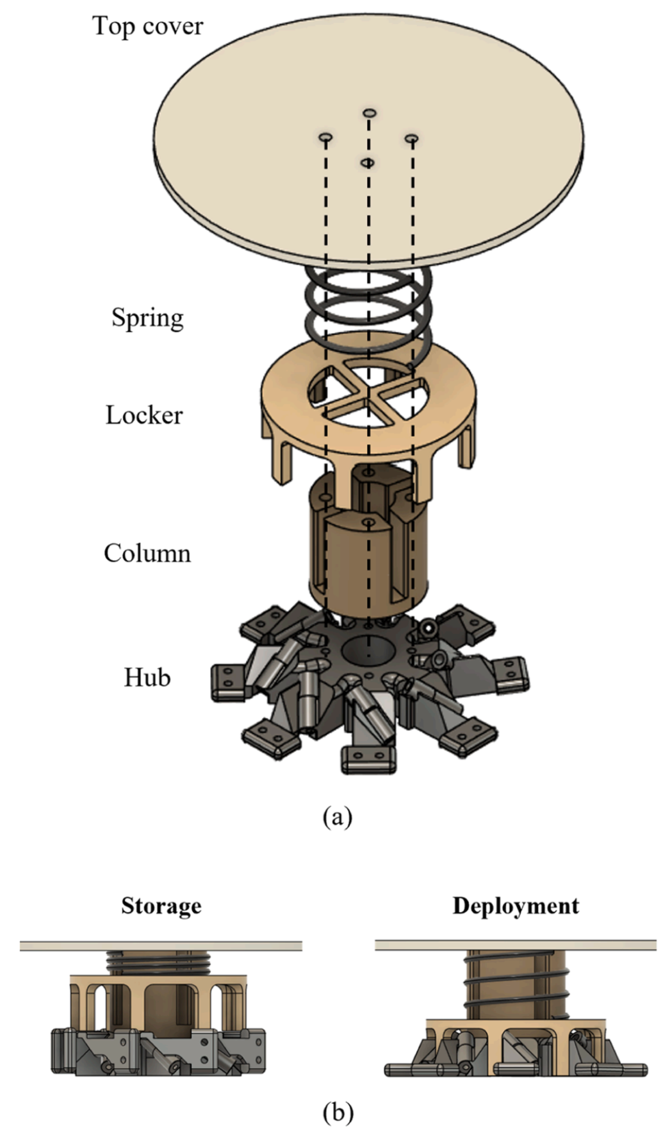

Fig. 7. (a) Overall hub component. (b) Design of locking mechanism.

Since the rotation axis is the eigenvector of the rotation matrix with an eigenvalue of 1, the rotation axis of the rotation matrix **R** is along the vector $\boldsymbol{d} = (-1,\ -1,\ 1)$ based on the frame {s}. The rotation moves the point **C** along the arc of a circle to **C'**. The rotation angle, θ, is determined to be 120° from the trace of the matrix R, which is given by an extension of the Rodrigues' formula as shown in (4) [39].

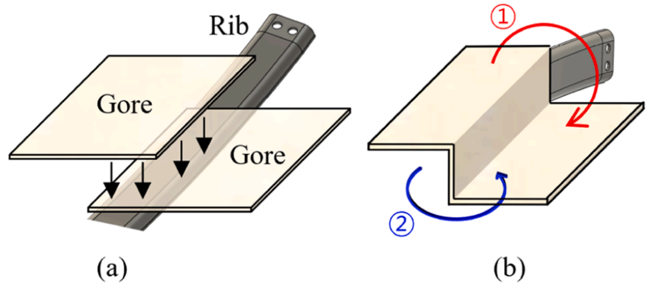

Fig. 8. Shape of the rib and the cross section.

$$\mathrm{Tr}(\boldsymbol{R}) = 1 + 2cos(\theta) \tag{4}$$

In the top view of the stowed state, the root of the rib is almost tangential to the hub due to the hinge structure. Thus, the equation of the Archimedean spiral can be utilized to evaluate the feasibility of storing the 500 mm reflector within a 1 U CubeSat. The stowed configuration of a single rib can be depicted using (5) where $r(\phi)$, N, a, and D_{hs} are polar coordinates of ribs in stowed state, the number of ribs, the spacing between stowed ribs, and the hub diameter in the stowed state, respectively [40].

$$r(\phi) = \frac{Na}{2\pi}\phi + D_{hs} \tag{5}$$

The design parameters are specified as $N = 8$, $a = 2.5$ mm, $D_{hs} = 50$ mm as shown in Fig. 6. A numerical method is employed to calculate the rib length as a function of the angle ϕ by using MATLAB. The generation of the spiral curve is terminated once the calculated length reaches its predefined value (241 mm). using MATLAB for the prototype. The stowed configuration of two ribs is shown in Fig. 6. The empty space in the center, with a diameter of 50 mm, corresponds to the hub diameter in the stowed state. This demonstrates that the storage ratio is 500 mm / 96 mm = 5.2, which is calculated as the diameter of the deployed state divided by that of the stowed state.

A locking mechanism for the hub is designed to enhance structural integrity and surface accuracy. The overall hub component consists of the hub, hub column, locker, spring, and top cover, which are assembled sequentially as shown in Fig. 7(a). The locking mechanism is positioned on the hub and the locker uses the hub column as a guide to slide vertically. The detailed design of the locking mechanism is shown in Fig. 7(b). After the antenna is released, a spring (0.98 N/mm) presses the locker downward, and the locker constrains the angular displacement to secure rotating parts in place. This mechanism effectively eliminates any slack resulting from the clearance fit of the rotating part, thereby maintaining the ribs in a deployed state during orbital vibrations.

Additionally, the geometric consequence of a rotational error on a rib is analyzed in consideration of potential assembly or manufacturing faults. The resulting deviation in rib height was quantified at five equidistant points along the rib's length by using 3D CAD software. For this assumed 1° rotational error, the RMS error was determined to be 1.50 mm. This result indicates that even a 1° rotational error across all ribs would likely introduce a significant increase to the overall RMS surface error. Therefore, it is important to achieve high precision during manufacturing and assembly to ensure the final surface accuracy of the structure.

3.2. Geometry of rib

The rib is a component that connects both the hub and the reflective surface, playing a crucial role in maintaining the shape of the antenna. As depicted in Fig. 8, one end of the rib is connected to the rotating part of the hub, while the remainder is attached to gores. The rib has curvatures in two directions to adjust stiffness since the rib requires both flexibility for stowage and adequate stiffness to maintain the deployed

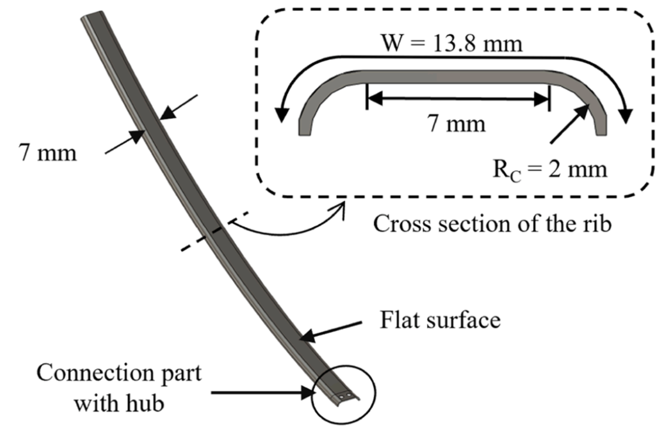

Fig. 9. (a) Connection between the rib and the gores. (b) The sequence of rotation during the stowing process: ① The rib is rotated to be perpendicular to the gore. ② The rib is wrapped around the hub for stowing.

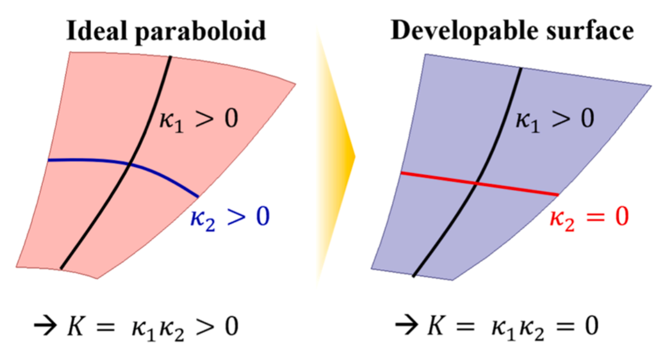

Fig. 10. Conversion of the paraboloid into a developable surface to simplify fabrication.

shape. The rigidity varies according to the curvature radius R_C and width W of its cross-section.

The design parameters of the rib were determined based on functional requirements. To prevent geometric interference with the hub's connection interface, the rib's cross-section has a 7 mm-wide flat part and a curvature radius of 2 mm. For a 0.25 mm thick polyethylene terephthalate (PET) sheet, the cross-sectional width is established at 13.8 mm after testing ribs with widths that are incrementally increased in 0.4 mm steps. This dimension represents the maximum width that allows the rib to be stowed around a 50 mm diameter hub without undergoing permanent deformation.

Fig. 9(a) shows the method of connecting the rib and the gores, where the two components are attached in parallel, effectively preventing torsion. They are initially attached using double-sided tape and securely fastened by stitching with wires. The sequence of rotation during the stowing process is shown in Fig. 9(b). As the stowing begins, the rib rotates to become perpendicular to the gore and then wraps around the hub to form the stowed configuration.

2.3. Geometry of gore

The gore is a segment of the reflective surface, divided according to the number of ribs. While an ideal reflector requires the continuous double curvature of a paraboloid, the flexible mesh is geometrically constrained to form a developable surface when tensioned between the ribs. A developable surface is defined as a surface with zero Gaussian curvature, allowing it to be unfolded into a flat plane without any distortion. K, κ_1, and κ_2 denote the Gaussian curvature, the principal curvature in the radial direction, and the principal curvature in the

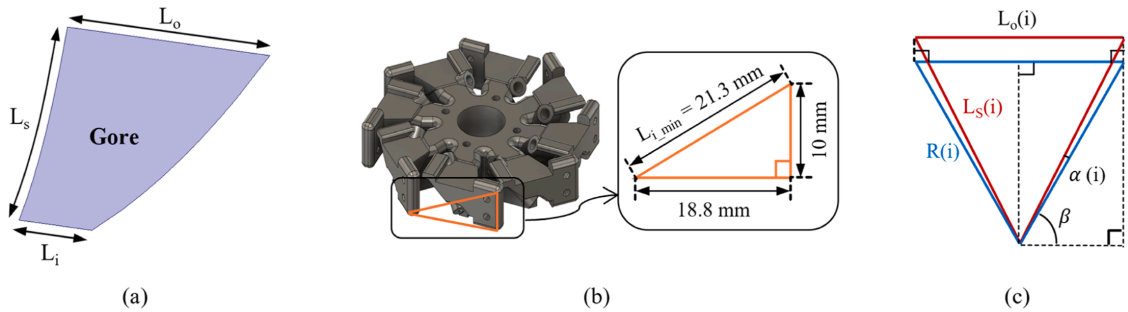

Fig. 11. (a) Three design parameters of the gore. (b) Calculation of L_{i_min} from the shape of the hub in the stowed state. (c) Calculation of α for each small displacement in R.

circumferential direction, respectively. The Gaussian curvature ($K = \kappa_1\kappa_2$) of a gore with an ideal parabolic surface and that of a gore with a developable surface are shown in Fig. 10. This conversion reduces κ_1 to zero, resulting in a gore with zero Gaussian curvature.

Although this process may lead to a reduction in surface accuracy, this limitation can be solved by employing a sufficient number of ribs. For example, a simple analysis, which sampled the surface deviation profile at ten equidistant points along the centerline of a gore, confirms that the eight-rib configuration achieves an RMS error of approximately 4.5 mm, thus meeting the criterion (9.55 mm) with a substantial margin.

For the design of the gore layout, it is essential to accurately calculate the length of the edges that define the boundary of each gore. Fig. 11(a) shows the design parameters of the gore where L_i is the length of the edge closest to the hub, L_o is the length of the edge furthest from the hub and L_s is the length of the curved sides of the gore.

L_o is a value determined by

$$L_0 = d\sin\left(\frac{\pi}{N}\right) \tag{6}$$

where d is the diameter of the reflector and N is the number of ribs. The prototype antenna in this study is an octagon inscribed in a circle with a diameter of 500 mm when viewed from the top view, which means L_o is about 191 mm.

L_i is a critical value to ensure the complete stowage of the antenna. A smaller L_i is preferable for achieving higher surface accuracy. However, stowage is impossible if L_i is too small. The material for the gore is usually a thin metal mesh with a wire. Since the material is characterized by its low strain tolerance, it is assumed that the relative distance between any two points may decrease but will not increase. Consequently, if the length of the edge is too short, it could result in damage to the reflector or render stowing impossible. The minimum L_i can be calculated using the dimensions of the hub in its stowed state. As shown in Fig. 11(b), the minimum L_i is indicated as L_{i_min}, which can be determined using the Pythagorean theorem. The minimum L_i is calculated to be $\sqrt{18.8^2 + 10^2} = 21.3$ mm, but a larger value of 25 mm is selected for safety margin.

L_s is the length of the parabolic curve in the cross-section of the reflector's front view. The length is calculated by (7) where f is the focal length of the parabola and R is the radius of the reflector in the top view. For the numerical analysis, the entire structure was discretized into hundreds of segments and the index i denotes the i th segment. The angle between the edges on both sides of a gore also needs to be figured out by calculating α, which is the difference of angle between the blue and red lines for each small displacement in R as shown in Fig. 11(c). The blue boundary represents the top view of a single gore of the parabolic reflector, while the red boundary represents the top view of the flattened gore. (8) is derived from the fact that the length of L_o is fixed, and β is defined by the number of gores, N, which is expressed as (9). Finally, α can be determined by substituting (9) into (8).

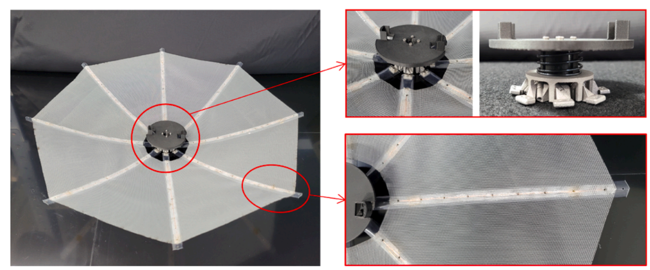

Fig. 12. Fabricated prototype of the mesh reflector.

$$\begin{aligned} L_s(i) &= \int_0^{R(i)} \sqrt{1 + \left(\frac{dz}{dr}\right)^2}\, dr \\ &= \frac{R(i)}{2}\sqrt{1 + 4\left(\frac{1}{4f}\right)^2 R(i)^2} + f\,\sinh^{-1}\left(\frac{1}{2f}R(i)\right) \end{aligned} \tag{7}$$

$$L_s(i)\cos(\beta + \alpha(i)) = R(i)\cos(\beta) \tag{8}$$

$$\beta = \frac{\pi}{2} - \frac{\pi}{N} \tag{9}$$

Through this process, the boundary of the gore can be accurately calculated. Additionally, a specific pre-strain is induced in gores to ensure surface accuracy. This is achieved by fabricating the gores with a width reduced by 2 % relative to the final spacing of the ribs. This intentional control creates a uniform tension across the mesh when it is attached to the ribs.

4. Performance validation

4.1. Reflector fabrication

The prototype of the mesh reflector is presented in Fig. 12. The hub component is manufactured using 3D printers. The hub and hub column are made of Aluminum, and the others are made of Onyx filament. Ribs are first made by laser-cutting PET according to the design of the rib. Then, the cut PET is placed between 3D-printed jigs and thermoformed in an oven at 100 °C for 30 min. The gore is cut to the shape of the defined dimensions. The reflective surface for the system-level deployment test, which includes ejecting components and feed antenna, is made of fabric mesh to focus on the dynamics of the proposed deployment mechanism. For the surface accuracy analysis and radiation pattern measurement, the reflective surface is fabricated using tungsten mesh. It has 13 openings per inch (5.12 openings per cm) and is knitted from tungsten wire with a diameter of 50 μm

Additionally, the accuracy of the gore length can be evaluated in the context of manufacturing tolerances. According to industry standards,

Table 2
Comparison of storage ratios between reflectors for CubeSat.

	Proposed antenna	Tension truss antenna [19]	Fold rib antenna [20]	Wrapped rib antenna [21]
Deployed diameter [m]	0.5	1	0.5	0.5
Storage volume	1U	3U	1.5U	1.5U
Storage ratio in diameter	5	10	5	5
Storage ratio in height	2.6	1	0.4	1

fiber laser systems typically achieve cutting tolerances of approximately ±0.025 mm. The metal mesh used in this study barely stretches in the longitudinal direction, which prevents a significant impact on surface accuracy.

Finally, the hub's rotating parts and rib's root are assembled using mechanical fasteners, and the gores are attached to the ribs by applying double-sided tape and stitching with 1 mm thick copper wire. And then, the locking mechanism is assembled sequentially. The proposed prototype with metal mesh has a mass of 66.7 g without the feed antenna, which accounts for 3.34 % of the standard 2 kg mass allocation for a 1 U CubeSat [41]. The geometrical characteristics of the proposed reflector mechanism are summarized and compared with three other reflector mechanisms for CubeSat as shown in Table 2. This comparison is based solely on the dimensions of the reflector and represents that the proposed reflector mechanism has the smallest storage volume.

4.2. Deployment test

The antenna deployment system and a 1 U CubeSat model were designed for deployment tests. A dummy feed antenna, support struts, and the ejection system were prepared also. It is connected to the deployable mesh reflector by two tape-spring struts. The length of the strut is determined based on the focal ratio.

The chassis of the CubeSat model is made of acrylic, and a spring is installed at the bottom of the cube to eject the antenna. Four linear guides that are positioned at the four corners prevent the antenna from tilting during ejection. For locking the cube cover in the stowed state, a servo motor and a wire are mounted on the side of the cube and connected to each other. When triggered, the servo motor rotates to open the cube cover like a double-hinged door.

Once the stowed antenna ejects from the cube, the mesh reflector expands due to the elasticity of the ribs, and the restoring force of the tape-spring struts positions the feed antenna at the focal point. The front view and isometric view of the deployment process of the prototype are shown in Fig. 13(a), Fig. 13(b) and supplementary content, Movie S1.

Additionally, the reaction torque profile exerted on CubeSat was measured during deployment. Fig. 14(a) shows the setup for the measurement. A torque sensor, RFT60-HA01-D, made by ROBOTOUS is integrated at the base of the reflector and the results for 5 deployments are shown in Fig. 14(b). Measurements show that deploying the prototype causes a transient disturbance to the CubeSat, resulting in a peak reaction torque of 0.22 N·m on average. To assess the risk of satellite attitude disturbance, the angular velocity is calculated across the critical phase, specifically from the initiation of a discernible torque impulse (164 ms) to the point at which the change in torque reaches saturation (275 ms). First, the angular impulse, H, is obtained as −0.000549 N·m·s by integrating the torque with respect to time.

The moment of inertia, I, of the 3 U CubeSat (6 kg) is calculated as in (10) under the assumption that the reflector is deployed at the CubeSat's apex.

$$I = \frac{1}{12} \times m \times \left(a^2 + b^2\right) = \frac{1}{12} \times 6\ \text{kg} \times \left(0.1^2\ \text{m}^2\ + 0.1^2\ \text{m}^2\right) = 0.01\ \text{kg·m}^2 \tag{10}$$

where m is the mass, and a and b are the side lengths of the CubeSat perpendicular to the axis of rotation. The angular velocity, $\Delta\omega$, is obtained:

$$\Delta\omega = \frac{\text{H}}{\text{I}} = \frac{-0.000549\ \text{N·m·s}}{0.01\ \text{kg·m}^2} = -0.0549\ \text{rad}\Big/s = -3.14\ ^{\circ}\Big/\text{s} \tag{11}$$

The calculated value is within the maximum permitted initial

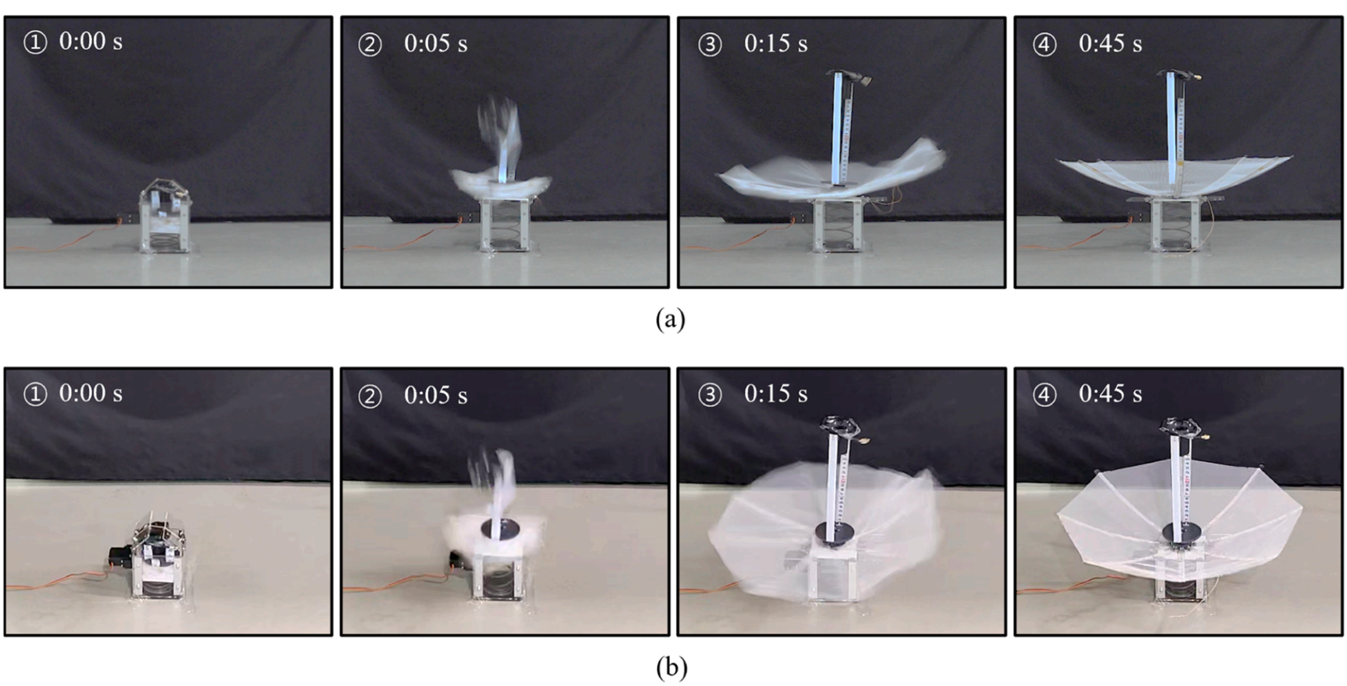

Fig. 13. Antenna deployment test. (a) Front view. (b) Isometric view.

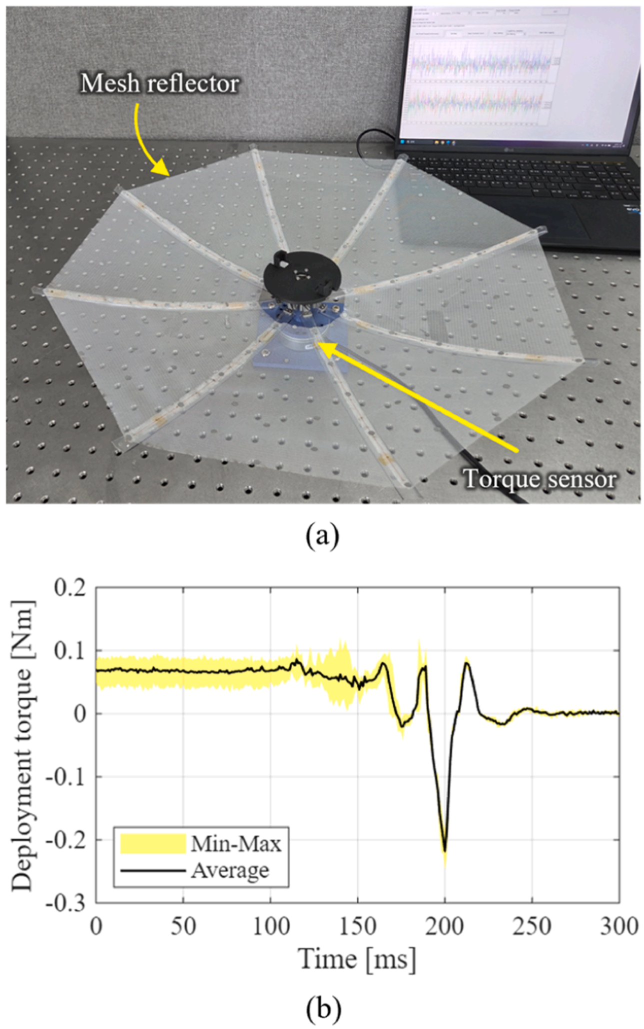

Fig. 14. (a) Deployment torque test setup. (b) Torque measurement result.

angular velocity for detumble operations which is 10 °/s per axis [42]. Therefore, the proposed antenna's deployment, which induces this angular velocity, can be managed by the CubeSat's attitude determination and control system.

4.3. Surface accuracy measurement

The surface accuracy of the reflector was measured to assess the gain loss. As shown in Fig. 15(a), 112 measurement points are evenly distributed on the reflective surface. The 3D Cartesian coordinates of each point are obtained using four Prime Cameras from OptiTrack for motion capture. After that, the coordinates were converted to cylindrical coordinates, and the z-axis values of the measured points were compared with the z-axis values of the ideal reflector. RMS error, σ_{rms}, is calculated using (12) where N and Δz are the total number of points and the error between the z-axis values of the measured points and the ideal parabolic surface, respectively [43]. The measured average error and σ_{rms} were measured to be 0.96 mm and 2.83 mm before deployment. They increased to 3.92 mm and 5.41 mm following deployment. The corresponding surface error distributions are illustrated in Figs. 15(b) and 15(c), respectively. In two subsequent deployments, the RMS errors were recorded as 6.55 mm and 6.18 mm. The convergence of these RMS error values suggests that the deployment process is repeatable. Furthermore, the observed degradation can be mitigated by using thinner metal mesh and stiffer ribs, which are real space-grade.

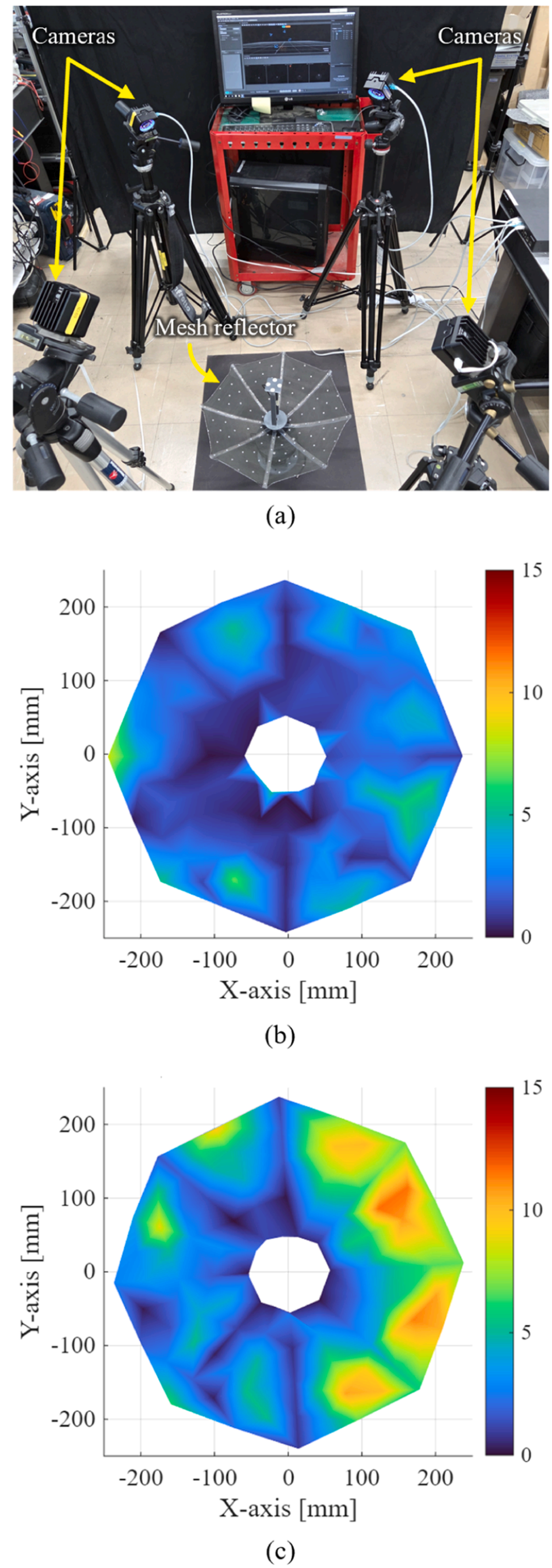

Fig. 15. (a) Surface accuracy measurement of the mesh reflector. (b) Measured surface error distribution before deployment test. (c) Measured surface error distribution after the first deployment test.

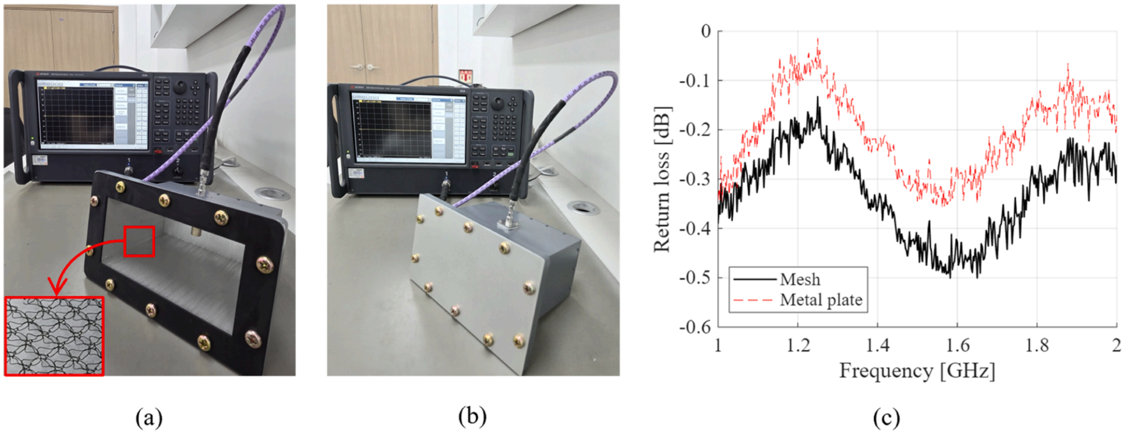

Fig. 16. (a) Return loss (S_{11}) measurement of 1 mm thick aluminum plate. (b) Return loss (S_{11}) measurement of tungsten mesh. (c) Measurement results of aluminum plate and tungsten mesh.

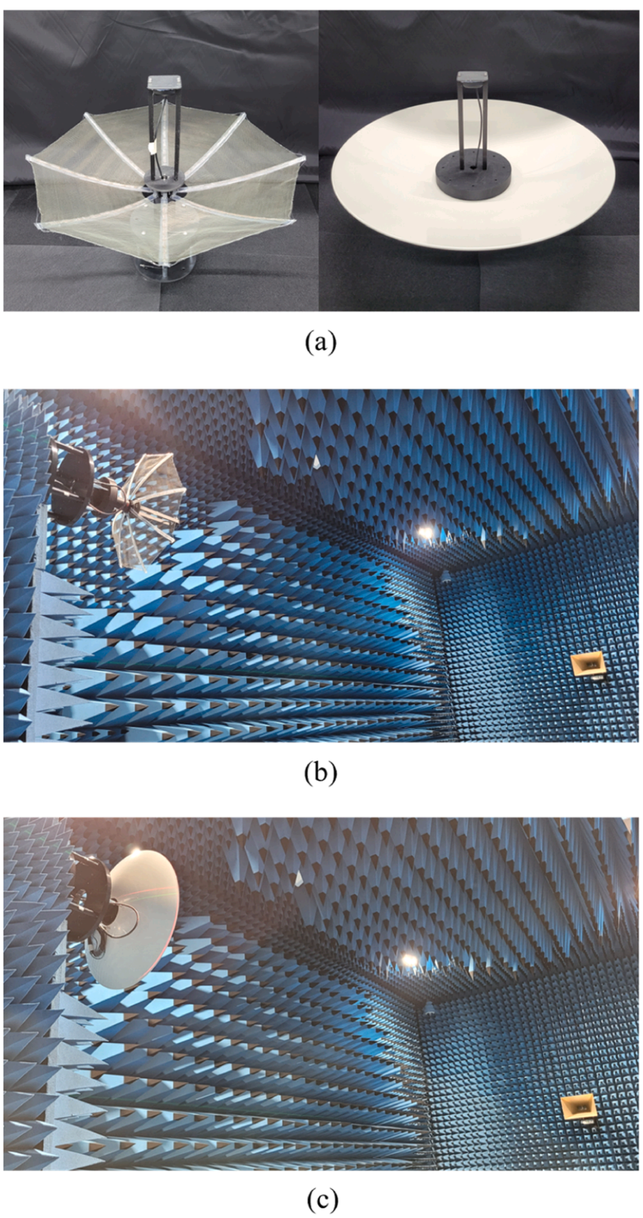

Fig. 17. (a) Mesh and solid reflector antenna. (b) Radiation pattern measurement of mesh antenna. (c) Radiation pattern measurement of solid antenna.

$$\sigma_{rms} = \sqrt{\frac{1}{N}\left(\sum_{k=1}^{N} \Delta z_i^2\right)} \tag{12}$$

4.4. Radiation pattern measurement

The electric performance of the proposed deployable mesh reflector antenna was evaluated in comparison to that of a solid reflector antenna. At first, the return loss (S_{11}) of the mesh was measured by using an L-band waveguide, UIYWTCWR650A113T173, made by UIY, and a vector network analyzer (VNA), E5080B, made by KEYSIGHT. One-port VNA calibration is conducted using a Keysight ECal module, N4691D, from 1 GHz to 2 GHz with 401 points, after which the waveguide is connected to the calibrated port. S_{11} was measured for two distinct configurations: with a Tungsten mesh placed over the same aperture and secured using a non-conductive jig as shown in Fig. 16(a); with a 1 mm-thick solid aluminum plate fixed at the waveguide aperture as shown in Fig. 16(b). A comparison of the two results revealed a maximum deviation of approximately 0.15 dB in the S_{11} values, which confirms that the mesh behaves as an effective electrical conductor, nearly identical to a solid metal plate.

The solid reflector is made of aluminum. Both mesh and solid reflectors have the same diameter and focal ratio. However, the solid reflector features an ideal parabolic surface, whereas the mesh reflector is divided into eight gores as shown in Fig. 17(a). A commercial GPS passive antenna, PE51066–1 (PASTERNARK), is used for the feed antenna. The tape-spring struts, which are used in the deployment test, are replaced with 3D-printed solid struts to compensate for deflection caused by gravity. The feed antenna has a gain of 3 dBi with an axial ratio (AR) of 3 dB and operates in right-hand-circular polarization (RHCP). Since the polarization inversion is caused by the reflector, the performance of left-hand-circular polarization (LHCP) is measured for the entire reflector antenna system. The radiation pattern of both antennas was measured in a far-field antenna measurement facility at Wireless Communication Convergence Support Center located in Daejeon, South Korea as shown in Fig. 17(b) and Fig. 17(c). The antenna measurement system for the far-field range, MS10040, is made by C&G Microwave.

The measured normalized gain patterns of the mesh and solid reflector antennas are shown in Fig. 18(a) and Fig. 18(b), for horizontal ($\varphi = 0°$) and vertical ($\varphi = 90°$) plane, respectively. Fig. 18(c) shows the AR for each reflector, exhibiting a similar trend across theta (θ). Table 3 summarizes the directivity, half-power beam width (HPBW), and AR of the mesh and solid reflector antennas at 1.57 GHz.

The difference in directivity between mesh and solid reflectors is 1.07 dB, which results from disparities in antenna aperture and surface

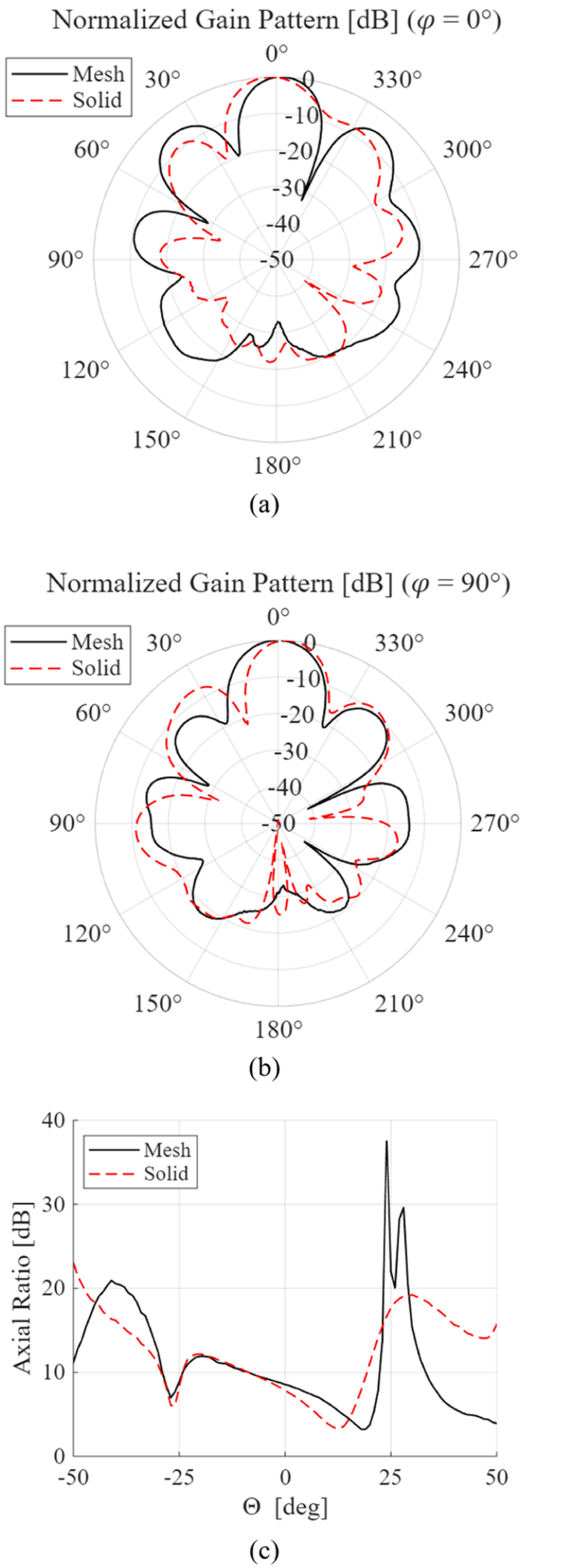

Fig. 18. (a) Normalized radiation pattern at $\varphi = 0^{\circ}$. (b) Normalized radiation pattern at $\varphi = 90^{\circ}$. (c) Axial ratio.

Table 3
Measurement results of radiation pattern at 1.57 GHz.

	Directivity	HPBW ($\varphi = 0^{\circ}$)	HPBW ($\varphi = 90^{\circ}$)	AR
Mesh	13.07 dBi	19.42°	22.31°	8.54 dB
Solid	14.14 dBi	19.644°	22.43°	7.86 dB

accuracy. The area of an octagon with a diagonal length of 0.5 m is 0.176 m^2, whereas the area of a circle with a diameter of 0.5 m is 0.196 m^2. Assuming equal aperture efficiency, the loss due to different aperture δ_a is calculated as 0.47 dB using (1). The loss caused by surface accuracy measurement after the first deployment, δ_{rms}, was 0.55 dB in accordance with (2). The combined theoretical loss of 1.02 dB closely matches the measured difference. Additionally, the half-power beam widths of the two antennas are nearly identical.

The axial ratio differs by 0.68 dB between the two antennas, which is caused by the surface RMS error of the deployable mesh reflector. Additionally, the elevated AR of each antenna is attributed to electromagnetic scattering from the solid struts, which is located within the near-field of the feed antenna. The presence of this dielectric composite introduces unwanted scattering of the signal radiated from the feed, which degrades the axial ratio. This issue can be mitigated by using a thin, non-conductive tape-spring.

This analysis confirms that the prototype's performance aligns closely with theoretical predictions, with the primary losses attributed to quantifiable geometric and surface factors. Therefore, the results validate the fundamental feasibility of the proposed deployable mesh antenna mechanism.

5. Discussion

In this paper, a 1U-scale deployable mesh reflector antenna is presented to meet the increasing demand for GNSS-RO missions employing CubeSats. The cross-axis folding hinge is utilized for the hub design, which can change the angle of the rib. The reflective surface and the rib are connected in parallel in the deployed state, preventing the rib's bending in the wrapping direction. But they are facing each other vertically in the stowed state, reducing the angle between the hub and ribs. Thus, the proposed deployment mechanism enables the antenna to achieve geometrical stability and high storage ratio simultaneously.

The proposed deployable antenna mechanism has a storage ratio of 5.2 precisely, which allows the 0.5 m diameter reflector to be stowed in a 1 U cube. The measured RMS error of the current prototype is 5.0 mm, which is equivalent to about λ/38 at the frequency of 1.57 GHz. In the far-field measurements, it has a high directivity of 13.07 dBi, which shows a 61 % improvement compared to the Spire's commercial patch antenna for GNSS-RO missions. This result demonstrates the feasibility of the proposed deployment mechanism.

This study can contribute to the advancement of antenna technology for GNSS-RO CubeSat missions by addressing the key challenge of achieving high gain within strict volume constraints. The proposed mechanism represents a meaningful step toward enabling more frequent, and cost-effective GNSS-RO missions through constellations of small satellites. Moreover, the mechanism is adaptable to a wide range of CubeSat applications. For high-frequency systems, such as satellite communications and radar, the requested surface accuracy can be achieved by designing optimized feed antenna, refining the mesh resolution and increasing the number of ribs. This inherent adaptability makes the design a flexible and scalable solution capable of meeting diverse mission demands.

Future work will commence with the development of an optimized feed antenna, such as a microstrip patch or a helical antenna, which will be designed using 3D full-wave electromagnetic simulations. Subsequently, the reflector's design parameters will be optimized based on the feed's performance to maximize the overall system gain.

The proposed manufacturing method considers the properties of space-grade materials. Thus, although the current prototype is not space-grade, each component can be manufactured to meet space-qualified standards. Following the finalization of the antenna fabrication, a comprehensive structural and thermo-mechanical analysis will be conducted to ensure its viability for spaceflight applications. This analysis will verify the antenna's mechanical robustness under simulated launch and on-orbit environments, including vibration up to a maximum frequency of 2000 Hz [44], and thermal vacuum cycling with temperature range of around ±100 °C [45].

Potential issues such as surface deformation caused by microgravity effects and thermal expansion, as well as loosening of mechanical joints during launch, will be evaluated. These issues will be addressed by selecting low thermal expansion materials, adjusting the tension of the gores, and computing the required spring coefficient of the locking mechanism. Once these design and analysis phases are completed, the space-qualified prototype will be fabricated, and its operational feasibility will be validated considering space environments.

CRediT authorship contribution statement

Gagyeong Park: Writing – review & editing, Writing – original draft. **Dong-Wook Yang:** Methodology, Investigation. **Min-Woo Oh:** Methodology, Investigation. **Jang-Soo Chae:** Resources, Investigation. **Hyosang Yoon:** Conceptualization. **Jae-Hung Han:** Conceptualization. **Dae-Young Lee:** Writing – review & editing, Methodology, Conceptualization.

Declaration of competing interest

The authors declare that they have no known competing financial interests or personal relationships that could have appeared to influence the work reported in this paper.

Acknowledgements

This work was supported by: the National Research Foundation of Korea funded by the Ministry of Science and ICT under Grant 2022M1A3C2069728, Future Space Education Center; the National Research Foundation of Korea(NRF) grant funded by the Korea government(MSIT) (No. RS-2025-02213804); the BK21 FOUR Program of the National Research Foundation Korea (NRF) grant funded by the Ministry of Education (MOE); OnB Space Inc.

Supplementary materials

Supplementary material associated with this article can be found, in the online version, at doi:10.1016/j.ast.2025.110694.

Data availability

All data needed to support the conclusions of this manuscript are included in the main text. Additional data related to this paper may be requested from the authors.

References

[1] R. Newman, I. Noy, The global costs of extreme weather that are attributable to climate change, Nat. Commun. 14 (1) (Dec. 2023), https://doi.org/10.1038/s41467-023-41888-1.
[2] H. Gleisner, M.A. Ringer, S.B. Healy, Monitoring global climate change using GNSS radio occultation, NPJ Clim. Atmos. Sci. 5 (1) (Dec. 2022), https://doi.org/10.1038/s41612-022-00229-7.
[3] D. Svehla, Geometrical Theory of Satellite Orbits and Gravity Field, Springer, 2018.
[4] G. Beyerle, T. Schmidt, J. Wickert, C. Reigber, R. König, N. Jakowski, W. Hauschild, K.I. Foelsche, GPS radio occultation with GRACE: atmospheric profiling utilizing the zero difference technique, Geophys. Res. Lett. 32 (13) (Jul. 2005), https://doi.org/10.1029/2005GL023109.
[5] C. Arras, J. Wickert, G. Beyerle, S. Heise, T. Schmidt, C. Jacobi, A global climatology of ionospheric irregularities derived from GPS radio occultation, Geophys. Res. Lett. 35 (14) (Jul. 2008), https://doi.org/10.1029/2008GL034158.
[6] C.H. Chu, H. Cheng-Yung, F. Chen-Joe, S.Y. Chen, Y.H. Chen, W.H. Yeh, Y.H. Kuo, Atmospheric remote sensing using global navigation satellite systems: from FORMOSAT-3/COSMIC to FORMOSAT-7/COSMIC-2, TAO: Terrestr., Atmosph. Ocean. Sci. 32 (6) (Dec. 2021) 1, https://doi.org/10.3319/TAO.2021.11.15.02.
[7] M. Zhran, A. Mousa, Global tropopause height determination using GNSS radio occultation, Egypt. J. Remote Sens. Space Sci. 26 (2) (2023) 317–331, https://doi.org/10.1016/j.ejrs.2023.04.004.
[8] Y. Sun, et al., The status and progress of Fengyun-3E GNOS II mission for GNSS remote sensing, in: Proc. IEEE Int. Geosci. Remote Sens. Symp, 2019, pp. 5181–5184, https://doi.org/10.1109/IGARSS.2019.8899319.
[9] V. Knap, S. Beczkowski, L.K. Vestergaard, D.I. Stroe, Battery current and temperature mission profiles for CubeSats at low Earth orbit, IEEE Trans. Aerosp. Electron. Syst. 58 (5) (Oct. 2022) 4656–4668, https://doi.org/10.1109/TAES.2022.3164867.
[10] S. Jung, J.P. Choi, Reliability of small satellite networks with software-defined radio and enhanced multiple access protocol, IEEE Trans. Aerosp. Electron. Syst. 57 (3) (Jun. 2021) 1891–1902, https://doi.org/10.1109/TAES.2021.3050652.
[11] A. Poghosyan, A. Golkar, CubeSat evolution: analyzing CubeSat capabilities for conducting science missions, Progr. Aerosp. Sci. 88 (Jan. 2017) 59–83, https://doi.org/10.1016/j.paerosci.2016.11.002.
[12] A. Chin, R. Coelho, L. Brooks, R. Nugent, J. Puig-Suari, Standardization promotes flexibility: a review of CubeSats' success, in: presented at the *AIAA 6th Responsive Space Conference*, Los Angeles, CA, USA, 2008. Apr. 28–May 1.
[13] R.L. Bishop, D.A. Hinkley, D.R. Stoffel, D.E. Ping, P.R. Straus, T.R. Brubaker, First results from the GPS compact total electron content sensor (CTECS) on the PSSC2 nanosat, in: Proc. 26th Ann. AIAA/USU Conf. Small Sat. SSC12-XI-2, Aug. 2012 [Online]. Available: https://digitalcommons.usu.edu/smallsat/2012/all2012/82/.
[14] M.J. Talpe, V.A. Nguyen, S. Tomás, Initial polarimetric radio occultation results from Spire's nanosatellite constellation: satellite payload, collection, and calibration, Bullet. Am. Meteorolog. Soc. 106 (4) (Apr. 2025) E714–E734, https://doi.org/10.1175/BAMS-D-23-0314.1.
[15] Z. Mo, Y. Lou, W. Zhang, Y. Zhou, P. Wu, Z. Zhang, Performance assessment of multi-source GNSS radio occultation from COSMIC-2, MetOp-B/C, FY-3D/E, Spire and PlanetiQ over China, Atmos. Res. 311 (Dec. 2024) 107704, https://doi.org/10.1016/j.atmosres.2024.107704.
[16] E.R. Kursinski, G.A. Haj, S.S. Leroy, B. Herman, The GPS radio occultation technique, Terrestr. Atmosph. Ocean. Sci. 11 (1) (Mar. 2000) 53–114.
[17] J. Wickert, T. Schmidt, C. Marquardt, C. Reigber, K.H. Neumayer, G. Beyerle, R. Galas, L. Grunwaldt, GPS radio occultation with CHAMP: first results and status of the experiment. Vistas For Geodesy in the New Millennium: IAG 2001 Scientific Assembly, Budapest, Hungary September 2–7, 2001, 2002, pp. 273–278, https://doi.org/10.1007/978-3-662-04709-5_45.
[18] M. Alibakhshikenari, et al., A comprehensive survey of "metamaterial transmission-line based antennas: design, challenges, and applications, IEEE Access 8 (2020) 144778–144808, https://doi.org/10.1109/ACCESS.2020.3013698.
[19] N. Chahat, J. Sauder, M. Mitchell, N. Beidleman, G. Freebury, One meter deployable mesh reflector for deep-space network telecommunication at X-band and ka-band, IEEE Trans. Antennas Propag. 68 (2) (2019) 727–735, https://doi.org/10.1109/TAP.2019.2943394.
[20] N. Chahat, R.E. Hodges, J. Sauder, M. Thomson, E. Peral, Y. Rahmat-Samii, CubeSat deployable ka-band mesh reflector antenna development for earth science missions, IEEE Trans. Antennas Propag. 64 (6) (Jun. 2016) 2083–2093, https://doi.org/10.1109/TAP.2016.2546306.
[21] H. Zhang, M. Wu, P. Xiang, D. Wu, Z. Yan, Q. Cui, Design, analysis, and test of an ultra-compact X-band deployable wrap-rib antenna, Acta. Astronaut. 228 (Mar. 2025) 918–930, https://doi.org/10.1016/j.actaastro.2025.01.001.
[22] M. Sureda, et al., Design and testing of a helix antenna deployment system for a 1U CubeSat, IEEE Access 9 (2021) 66103–66114, https://doi.org/10.1109/ACCESS.2021.3075660.
[23] D. Kim, M. Hwang, G. Kim, S. Kim, Self-deployable circularly polarized phased Yagi–Uda antenna array using 3-D printing technology for CubeSat applications, IEEE Antennas Wireless Propag. Lett. 21 (11) (Nov. 2022) 2249–2253, https://doi.org/10.1109/LAWP.2022.3197359.
[24] M. Hwang, G. Kim, S. Kim, N.S. Jeong, Origami-inspired radiation pattern and shape reconfigurable dipole array antenna at C-band for CubeSat applications, IEEE Trans. Antennas Propag. 69 (5) (2021) 2697–2705, https://doi.org/10.1109/TAP.2020.3030908.
[25] F.A. Dicandia, S. Genovesi, A compact CubeSat antenna with beamsteering capability and polarization agility: characteristic modes theory for breakthrough antenna design, IEEE Antennas Propag. Magazine 62 (4) (Aug. 2020) 82–93, https://doi.org/10.1109/MAP.2020.2965015.
[26] Y. Zhang, et al., Design of deployable mesh reflector antenna based on cable-dome tensegrity structure, Structures 68 (Oct. 2024) 107150, https://doi.org/10.1016/j.istruc.2024.107150.
[27] B. He, L. Jia, K. Li, R. Nie, Y. Fan, G. Wang, Deployment dynamic modeling and driving schemes for a ring-truss deployable antenna, Chin. J. Mechan. Eng. 37 (1) (2024) 79, https://doi.org/10.1186/s10033-024-01065-x.
[28] C.M. Feng, T.S. Liu, A graph-theory approach to designing deployable mechanism of reflector antenna, Acta Astronaut 87 (2013) 40–47, https://doi.org/10.1016/j.actaastro.2013.01.019.
[29] D. Wu, M. Wu, P. Xiang, Z. Yan, Surface accuracy analysis and optimization design of rib-mesh paraboloidal antenna reflectors, Aerosp. Sci. Technol. 129 (Oct. 2022), https://doi.org/10.1016/j.ast.2022.107817.

[30] J. Du, F. Wang, H. Bao, D. Ge, Z. Ren, Form-finding and shape adjustment of cable-membrane reflectors, Acta Astronaut 205 (Apr. 2023) 213–224, https://doi.org/10.1016/j.actaastro.2023.02.002.

[31] D. Tian, H. Gao, L. Jin, R. Liu, Y. Zhang, C. Shi, J. Xu, Design and kinematic analysis of a multifold rib modular deployable antenna mechanism, Mechan. Sci. 13 (1) (Jun. 2022) 519–533, https://doi.org/10.5194/ms-13-519-2022.

[32] J.H. Lim, Y.B. Kim, I.S. Jang, H. Kim, H.U. Oh, Parabolic deployable mesh antenna with a hingeless system of superelastic SMA ribs and composite tape springs, Acta Astronaut 200 (Nov. 2022) 149–162, https://doi.org/10.1016/j.actaastro.2022.08.007.

[33] K.N. Urata, J.T. Sri Sumantyo, C.E. Santosa, T. Viscor, A compact C-Band CP-SAR microsatellite antenna for earth observation, Acta Astronaut 159 (Jun. 2019) 517–526.

[34] O.G.I. Yoshiro, J. Reveles, V. Fraux, and D.J. Ashley, "Deployable wrapped rib assembly," U.S. Patent 16/348,39, Nov. 28, 2019, https://doi.org/10.1016/j.actaastro.2019.01.030.

[35] M.C. Moreau, "GPS receiver architecture for autonomous navigation in high Earth orbits," Ph.D. dissertation, University of Colorado at Boulder, 2001. [Online]. Available: https://www.proquest.com/docview/251672988?pq-origsite=gscholar&fromopenview=true&sourcetype=Dissertations%20&%20Theses.

[36] W.L. Stutzman, G.A. Thiele, Antenna Theory and Design, Wiley, Hoboken, NJ, USA, 2012.

[37] D.J. Rochblatt, B.L. Seidel, Microwave antenna holography, IEEE Trans. Microw. Theory Tech. 40 (6) (1992) 1294–1300, https://doi.org/10.1109/22.141363.

[38] H. Cheng, K.C. Gupta, An historical note on finite rotations, J. Appl. Mech. 56 (1) (Mar. 1989) 139–145, https://doi.org/10.1115/1.3176034.

[39] K.K. Liang, "Efficient conversion from rotating matrix to rotation axis and angle by extending Rodrigues' formula," *arXiv preprint arXiv:1810.02999*, 2018, https://doi.org/10.48550/arXiv.1810.02999.

[40] N. Jiménez, R. Picó, V. Sánchez-Morcillo, V. Romero-García, L.M. García-Raffi, K. Staliunas, Formation of high-order acoustic Bessel beams by spiral diffraction gratings, Phys. Rev. E 94 (5) (2016) 053004, https://doi.org/10.1103/PhysRevE.94.053004.

[41] A. Johnstone, CubeSat design specification rev. 14.1 the CubeSat program, Cal. Poly SLO (2022) [Online]. Available: https://static1.squarespace.com/static/5418c831e4b0fa4ecac1bacd/t/62193b7fc9e72e0053f00910/1645820809779/CDS+REV14_1+2022-02-09.pdf.

[42] S.T. Bednarski, CubeSat attitude determination and control system (ADACS) characterization and testing for rendezvous and proximity operations (RPO), 2021.

[43] S. Li, Y. Fan, Q. Chen, Surface error distribution research in reflector antenna from the measured data, J. Spacecr Rockets 58 (2) (Mar. 2021) 589–594, https://doi.org/10.2514/1.A34826.

[44] Goddard Space Flight Center, General environmental verification standard (GEVS) for GSFC flight programs and projects, NASA (2013). GSFC-STD-7000[Online]. Available: https://standards.nasa.gov/standard/gsfc/gsfc-std-7000.

[45] European Cooperation for Space Standardization, Thermal testing: space product assurance. ESA Requirements and Standards Division, Jul. 2008. ECSS-Q-ST-70-04C[Online]. Available: https://ecss.nl/standard/ecss-q-st-70-04c-thermal-testing/.